Research Article

Nano Research
2020, 13(12): 3268–3277

ISSN 1998-0124 CN 11-5974/O4
https://doi.org/10.1007/s12274-020-3000-9

# Dual activated NIR-II fluorescence and photoacoustic imaging-guided cancer chemo-radiotherapy using hybrid plasmonic-fluorescent assemblies

Tao Chen, Lichao Su, Xiaoguang Ge, Wenmin Zhang, Qingqing Li, Xuan Zhang, Jiamin Ye, Lisen Lin, Jibin Song (✉), and Huanghao Yang (✉)

*MOE Key Laboratory for Analytical Science of Food Safety and Biology, College of Chemistry, Fuzhou University, Fuzhou 350116, China*



**Received:** 21 June 2020 / **Revised:** 19 July 2020/ **Accepted:** 20 July 2020

## ABSTRACT

Multimodal imaging in the second near-infrared window (NIR-II) guided cancer therapy is a highly precise and efficient cancer theranostic strategy. However, it is still a challenge to develop activated NIR-II optical imaging and therapy agents. In this study, we develop a pH-responsive hybrid plasmonic-fluorescent vesicle by self-assembly of amphiphilic plasmonic nanogapped gold nanorod (AuNNR) and fluorescent down-conversion nanoparticles (DCNP) (AuNNR-DCNP Ve), showing remarkable and activated NIR-II fluorescence (FL)/NIR-II photoacoustic (PA) imaging performances. The hybrid vesicle also exhibited superior loading capacity of doxorubicin as a superior drug carrier and efficient radiosensitizer for X-ray-induced radiotherapy. Interestingly, the accumulated hybrid AuNNR-DCNP Ve in the tumor resulted in a recovery of NIR-II FL imaging signal and a variation in NIR-II PA imaging signal. Dual activated NIR-II PA and FL imaging of the hybrid vesicle could trace drug release and precisely guided cancer radiotherapy to ultimately reduce the side effects to healthy tissue.

## KEYWORDS

radiotherapy, second near-infrared window (NIR-II), fluorescence imaging, photoacoustic imaging, plasmonic gold nanovesicle

## 1 Introduction

Cancer remains a significant global challenge to human health [1–6]. Although a large number of potential new cancer treatments have been explored, only limited success has been achieved due to the heterogeneity and complexity of tumors [7–10]. To fight cancer, innovative intelligent nanoplatforms with therapeutic and diagnostic capabilities are highly warranted [11–13]. Theranostics, a novel concept of simultaneous diagnosis and treatment technology, provide a practicable strategy for real-time monitoring and reflect the effects of treatment, and optimize the efficiency and safety of treatment strategies [14–17]. The treatment technology simplifies the entire drug development process and saves a significant amount of money for the entire medical system [18–20]. Therefore, a diagnostic probe that combines diagnostic imaging and therapeutic functions would be an excellent alternative to contrast agents and cancer treatment strategies rather than traditional single diagnostic functions [21–23]. Nanoparticle-based diagnostic probes have high encapsulation ability to achieve the goal of the cancer diagnosis and treatment, and can cover various reagents and drugs with different diagnostic and therapeutic functions [24–26].

Real-time and accurate imaging is of utmost importance for the diagnosis and prognosis of various diseases [27–30]. Among them, fluorescence (FL) imaging has shown superior performance with high temporal resolution and high sensitivity, however, its use in the clinic is limited due to low tissue penetration depth [31, 32]. Compared to conventional FL imaging in the visible and near-infrared spectrum window of 400–900 nm, FL imaging probes have attracted increased attention in the second near-infrared window (NIR-II, 900–1,700 nm) due to excellent performance, including deep-tissue penetration, negligible auto FL and high spatial resolution [25, 33]. Optical probes with excellent performance, including single-walled carbon nanotubes (SWCNTs) [34–36], rare-earth doped nanoparticles [37, 38], silver chalcogenide quantum dots (QDs) [39, 40], and organic dyes [41–43], are promising candidates for both preoperative diagnosis and intraoperative guidance. Among the NIR-II FL probes, lanthanide ($Ln^{3+}$)-doped down-conversion nanoparticles (DCNPs) have many excellent characteristics, including low toxicity and high photo-stability [15, 44]. Therefore, DCNP are widely applied for *in vitro* bioassays and *in vivo* bioimaging.

Although NIR-II FL imaging for diagnostic purposes has been successfully developed, different spatial resolutions and scales information of the tumor cannot be completely studied by a single imaging mode [45]. Photoacoustic (PA) imaging is a hybrid imaging method that combines the advantages of optical imaging and ultrasound imaging [46, 47], which has demonstrated a deeper tissue penetration when compared to NIR-II FL imaging [48, 49]. In addition, deep tumor features can be obtained using PA imaging with microscopic spatial resolution, which is difficult to achieve with FL imaging [43, 50, 51]. Considering the advantages of each imaging modality,

Address correspondence to Huanghao Yang, hhyang@fzu.edu.cn; Jibin Song, jibinsong@fzu.edu.cn

the integration of NIR-II FL imaging and NIR-II PA imaging could provide accurate and rich information by compensating for inherent limitations, and each type of imaging would improve the accuracy of cancer diagnosis. Therefore, the rational design and manufacturing of integrated NIR-II FL/NIR-II PA bimodal imaging-guided cancer multimodal therapy is well-suited for the urgent need for accurate diagnosis and accurate and effective cancer treatment.

To date, many composite materials with excellent optical properties have been developed, which have been successfully applied in chemotherapy. However, after chemotherapy treatment, residual cancer may relapse due to the acquired drug resistance, which may reduce the effects of subsequent tumor treatment [1, 47]. Radiotherapy is another widely used method in the clinic for cancer treatment, which destroys tumor cells by X-ray radiation [52]. Radiotherapy can effectively prevent drug resistance caused by chemotherapy [53, 54]. Fortunately, an effective combination of chemotherapy and radiotherapy (chemo-radiotherapy) can take advantage of both treatments to improve anti-tumor effects [55–57]. Moreover, radiation therapy with precise imaging guidance has been shown to have minimal side effects to healthy tissues [58]. Therefore, establishing responsive NIR-II bimodal imaging methods to accurately guide the location of the tumor, and combine chemo-radiotherapy to reduce damage to healthy tissue and increase the anti-tumor effects is highly meaningful and clinically valuable.

Herein, we developed a new type of pH-activated vesicles by self-assembly of nanogapped gold nanorod (AuNNR) and DCNPs coated with PEG and pH responsive poly(methyl methacrylate-co-4-vinylpyridine, 25% 4VP) (PMMMVP), which were loaded with doxorubicin (DOX) and had high efficiency for integrated chemo-radiotherapy (Fig. 1). The resulting hybrid vesicle, DOX loaded pH responsive Ve, not only acted as a NIR-II FL/PA dual-modal imaging contrast agent, but also served as a chemo-radiotherapy agent. The AuNNR served as a competition absorber to filtrate photons at 980 nm excitation energy, thereby causing quenching of 1,550 nm emission of DCNP [31]. Subsequently, dissociation of the hybrid vesicle under acidic conditions caused the release of DCNP and recovery of its NIR-II FL signal, which allowed for a higher signal-to-noise ratio of the imaging, and resulted in an excellent bimodal NIR-II FL and NIR-II PA imaging effects. The accumulation of the hybrid Ve in the tumor region resulted in a significant increase of both NIR-II FL and NIR-II PA signals. Thus, the tumor size and location could be accurately observed via NIR-II FL/PA dual-modal imaging, which provided real-time monitoring of the therapeutic treatment effect, and prevented unwanted damage to healthy tissue. Furthermore, histological examination showed little to no noticeable toxic side effects of the Dox loaded Ve in healthy organs. Taken together, our *in vitro* and *in vivo* experimental results showed that the hybrid Ve demonstrated high anti-tumor efficacy due to the synergistic effects of controlled release of chemotherapeutics and imaging guided precise radiotherapy triggered by X-ray.

## 2 Experimental

### 2.1 Synthesis of Au nanorods (Au NRs)

The Au NRs were synthesized using a typical method. First, 5 mL $HAuCl_4$ (5 mM) and 5 mL cetyltrimethylammonium bromide (CTAB) (5 mmol) were mixed in 100 mL flask. After adding 50 mL distilled (DI) water, 100 μL $AgNO_3$ (0.1 M) solution was slowly added. After stirred for 10 min, 560 μL AA (0.1 M) solution and 40 μL $NaBH_4$ (1.6 mM) solution were added, and the mixture was stirred for 90 min. The resulting solution was centrifuged at 15,000 rpm for 10 min. The precipitate was repeatedly washed with DI water under sonication and re-dispersed in DI water for next experiment.

### 2.2 Preparation of the AuNNR

Briefly, the as-prepared AuNRs were dispersed in a 50 mL polyvinylpyrrolidone (PVP) (1%, MPVP/MDI water) solution. Then, 5 mL CTAB (0.1 M) was added in the solution, followed by adding 1.5 mL $AgNO_3$ (0.4 mM), 1.25 mL AA (0.1 M), and 0.25 mL NaOH (0.1 M) solutions, respectively. After stirred for 30 min, the Ag shell coated AuNR (AuNR@Ag) was prepared. The product was then centrifuged at 9,000 rpm for 15 min.

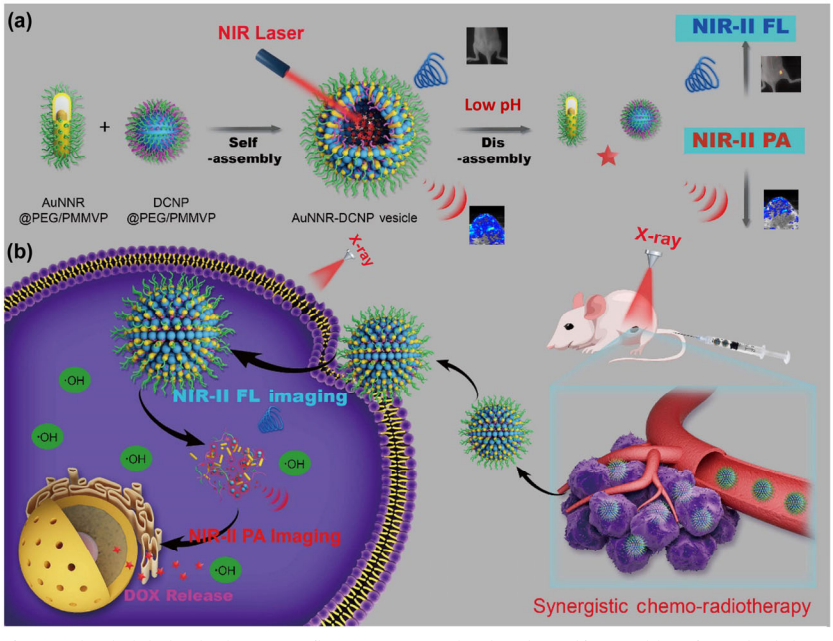


**Figure 1** (a) Preparation of DOX-loaded hybrid plasmonic-fluorescent vesicles by the self-assembly of amphiphilic AuNNR@PEG/PMMVP and DCNP@PEG/PMMVP. In an acidic environment, the vesicles were disassembled into single AuNNR and DCNP, leading to localized DOX release and responsive variation of NIR-II PA and FL signals. (b) Schematic illustration of the hybrid vesicle as a smart theranostic agent for accurate cancer chemo-radiotherapy-guided by dual NIR-II PA and FL imaging.

Then, the precipitate was washed with DI water under sonication and re-dispersed in 50 mL CTAB (0.1 M) solution. Next, 2 mL $HAuCl_4$ (0.01 mM) was sequentially added in this solution and stirred for 15 min. Finally, 1.25 mL AA (0.1 mM) was added in the mixture and stirred for 20 min. The products were purified by centrifugation at 9,000 rpm for 15 min and washed with DI water under sonication for three times. The obtained AuNNR was dispersed in DI water at 4 °C for following experiment.

### 2.3 Preparation of amphiphilic AuNNR@PEG/PMMVP

The pH responsive AuNNR was prepared by ligand exchange based on our previously reported method. In a typical procedure, 10 mM of AuNNR in 0.5 mL of DI water was dropped into 10 mL N,N-dimethylformamide (DMF) containing 5 mg PEG-SH and 5 mg PMMVP-SH solution under vigorous stirring. After reaction for 12 h, the AuNNR@PEG/PMMVP was obtained through centrifugation and washed with chloroform for three times.

### 2.4 Synthesis of amphiphilic DCNP@PEG/PMMVP

The DCNPs ($NaGdF_4$:Yb,Er) were firstly synthesized using a literature reported method. In brief, 0.78 mmol $Gd(CH_3COO)_3$, 0.20 mmol $Yb(CH_3COO)_3$, and 0.02 mmol $Er(CH_3COO)_3$ were added in a 100 mL flask with 15 mL 1-octadecene (ODE) and 6 mL cis-9-Octadecenylamine (OA). The mixture was slowly heated up to 150 °C for 30 min. After cooling to 50 °C, 10 mL methanol solution (contain with 2.5 mmol NaOH and 2.75 mmol $NH_4F$) was added to this solution and stirred violently for 30 min. Then, the solution was heated to 290 °C under argon for 60 min. After precipitating the products with ethanol, the $NaGdF_4$:Yb,Er nanoparticles were centrifugated at 6,000 rpm for 10 min, washed with ethanol under sonication for three times, and finally re-dispersion in chloroform. Then, 5 mg PEG-COOH and 5 mg PMMVP-COOH in 5 mL chloroform was added in the solution and reacted for 12 h. After centrifugation and washed by chloroform for three times, the amphiphilic DCNP@PEG/PMMVP was obtained and redispersed in chloroform.

### 2.5 Drug loading and release

To prepare DOX loaded vesicle, DOX, AuNNR@PEG/PMMVP and DCNP@PEG/PMMVP were mixed in 0.1 mL chloroform. Then the mixture was dropped into 1 mL PVA solution (0.5 mg/mL), and emulsified for 60 s by sonication. The mixed solution was centrifuged at 4,000 rpm for 5 min and washed with DI water for three times. To calculate the DOX release profile, the DOX loaded pH responsive Ve was exposed in DI water at pH 5.5. At predetermined time points, the DOX release behavior was tested and calculated using its characteristic absorption at 490 nm.

### 2.6 *In vitro* cytotoxicity of the pH-responsive nanoparticles

To study *in vitro* cytotoxicity of the pH-responsive vesicles. MCF-7 cells were seeded with a cell concentration of $1 \times 10^4$ cells/well in 96-well plate. After 12 h incubation, DOX loaded pH responsive Ve were added to each well in different concentrations ($n = 3$) with or without X-ray irradiation. Cell cytotoxicity was evaluated using Cell Counting Kit-8 (CCK-8) method with different treatments (with or without 5 Gy and 10 Gy of X-ray radiation) after incubation for 24 and 48 h.

### 2.7 *In vivo* NIR-II PA and FL imaging study

For *in vivo* NIR-II FL imaging, MCF-7 tumor bearing mice were tail vein injected with the hybrid vesicle (200 μL, 2 mg/mL), and using *In-Vivo* Master Laser imaging system to scan the real-time NIR-II imaging at different time points with an emission wavelength of 1,250 nm and excitation laser at 980 nm.

For *in vivo* NIR-II PA imaging, the mice were monitored by a vevo 3100 small animal imaging system at indicated time points after injection of the samples. And from the mean pixel values, the PA intensity at each time point for different organs (tumor and liver) were calculated.

### 2.8 *In vivo* cancer synergistic chemo-radiotherapy

All animal experiments were performed with the permission of the Animal Care and Use Committee of Fuzhou University. In order to evaluate the chemo-radiotherapy effect of DOX loaded pH responsive Ve *in vivo*, we estabilished the tumor model by subcutaneously injecting MCF-7 cells ($8 \times 10^6$) into the right back flank of mice. And mice were randomly divided into 6 groups, with different treatment before X-ray irradiation (5 and 10 Gy) at 24 h postejection, including (1) PBS (control group), (2) DOX, (3) DOX + X-ray irradiation, (4) DOX loaded pH responsive Ve, (5) DOX loaded none pH responsive Ve + X-ray irradiation, and (6) DOX loaded pH responsive Ve + X-ray irradiation. The tumor volume and body weight were recorded every two days until 18 days, and the tumor sizes were calculated by the equation: $V = \text{Length} \times \text{Width}^2/2$.

## 3 Results and discussion

### 3.1 Preparation of pH-responsive hybrid plasmonic-fluorescent vesicles

To prepare pH-responsive hybrid vesicles, DCNP of NaGdF4:Yb, Er, were firstly synthesized via a facile high-temperature co-precipitation method [57] (Fig. S1 in the Electronic Supplementary Material (ESM)). To prepare nanogapped gold nanorod, AuNRs with an approximate aspect ratio of 4 (approximate length: ~ 32 nm, approximately width: ~ 8 nm) were firstly mixed with an aqueous solution of PVP and CTAB (Fig. 2(a)). Following the addition of $AgNO_3$, an Ag layer was formed by ascorbic acid reduction to yield AuNR@Ag (Figs. S2(b) and S2(c) in the ESM). Then, AuNR@Ag was transformed to an AuNNR structure by adding $HAuCl_4$ to oxidize and substitute Ag through galvanic corrosion [9]. The AuNNR was formed with a hollow Au/Ag shell, which contained AuNR with a distinct gap (Fig. 2(b)). Finally, AuNNR grafted with PEG-SH and PMMMVP-SH through covalent Au–S bonds was prepared by a ligand exchange method (Fig. S2(e) in the ESM). Similarly, amphiphilic DCNP@PEG/PMMMVP was prepared by reaction between PEG-COOH/PMMMVP-COOH and DCNP. The balance of attractive force between hydrophilic PEG and hydrophobic PMMVP interactions guides the assembly of amphiphilic polymers with a bilayer structure mimicking the cell membrane through self-aggregation of their hydrophobic tails in an aqueous medium. Amphiphilicity-driven self-assembly of AuNNR@PEG/PMMVP and DCNP@PEG/PMMVP rose to hybrid vesicle with tailored mechanical and structural properties. During the self-assembly processes, the chemotherapy drug, DOX, was introduced into the internal cavity of the vesicle through a self-assembly method that was based on a previously reported method [59]. In brief, a predetermined ratio of AuNNR and DCNP was mixed in chloroform, following dropwise addition to a polyvinyl alcohol (PVA) solution. Next, the solution was emulsified by ultrasonic emulsification, followed by evaporation of the chloroform phase at 25 °C for 24 h, leading to generation of the hybrid vesicles. High resolution transmission electron microscopy (HRTEM) and energy-dispersive X-ray analysis (EDX) data clearly showed that hybrid vesicles consisted of

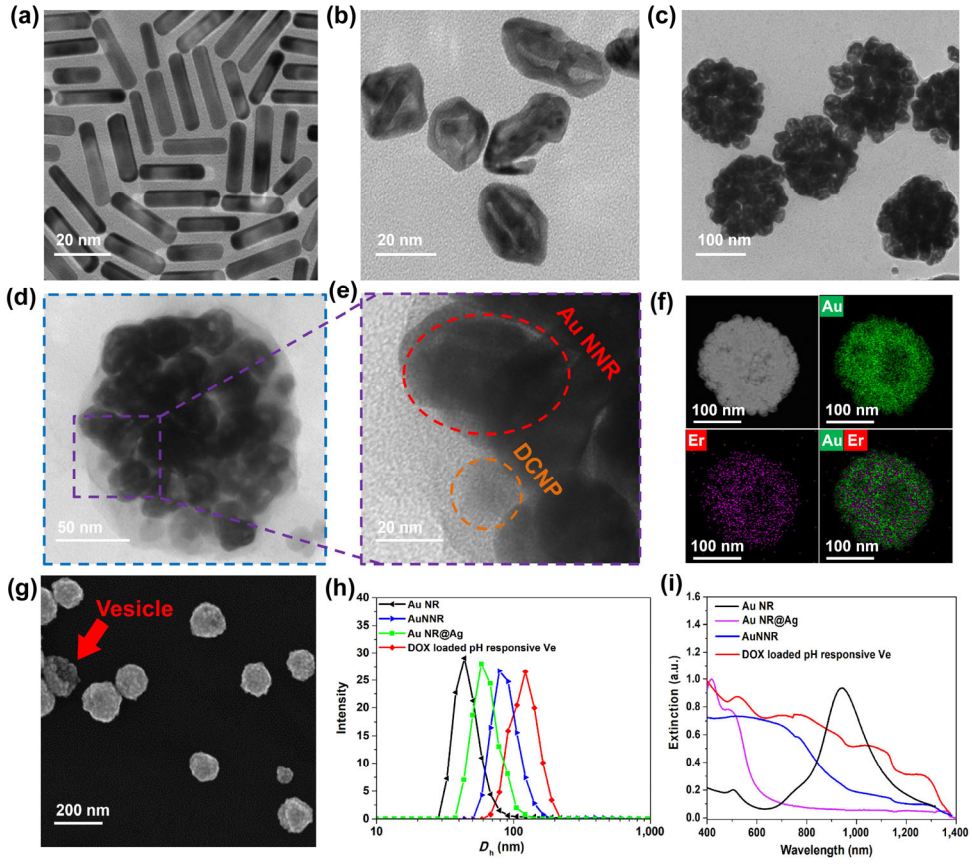


**Figure 2** TEM images of (a) AuNRs, (b) AuNNR, (c) the assembled hybrid vesicle, and HRTEM images of one hybrid vesicle (d) and (e), showing AuNNR and DCNP were colocalized in the vesicular shell. (f) EDS elemental mapping image and (g) Scanning electron microscopy (SEM) images of the hybrid vesicle. (h) Hydrodynamic distribution and (i) UV–vis spectra of AuNR, AuNR@Ag, AuNNR, and DOX loaded pH responsive Ve.

AuNNR and DCNP (Figs. 2(d) and 2(f)). The average diameter of the hybrid vesicle was about ~ 122 nm that was based on TEM and dynamic light scattering (DLS) results (Fig. 2(h)). Moreover, ultraviolet–visible (UV–vis) spectra were used to characterize the as-prepared AuNNR and hybrid vesicles. A broad absorption spectrum for hybrid vesicles was recorded (Fig. 2(i)), and the absorption peak of hybrid vesicles showed a significant red shift and displayed excellent NIR-II absorption when compared to that of AuNNR, which was due to the plasma coupling effect amount encapsulated AuNNR.

### 3.2 Activated NIR-II FL and PA properties of hybrid vesicles

We next investigated the pH-responsive disassembly behavior of the hybrid vesicles at acidic environments (Fig. 3(a)). After incubation with a pH 5.5 solution, the vesicles decomposed completely into AuNNR and DCNP (Fig. 3(b)). In addition, DLS data indicated the reduction in size of the hybrid vesicles during the disassembly process (Fig. S4 in the ESM). Subsequently, responsive NIR-II PA imaging performance of hybrid vesicles was further performed. Due to the strong plasmonic coupling of AuNR in the vesicular shell, the enhanced NIR-II light absorption of hybrid vesicles led to an enhanced PA signal. As expected, the PA images of hybrid vesicles were brighter compared to the images of AuNNR and DCNP, because of the optical enhancement effect of the assembled AuNNR (Fig. 3(c)). Moreover, the PA signals of hybrid vesicles were gradually decreased after treated with acidic solutions, because the disassembly of the vesicle and disappearance of the plasmonic coupling effect (Fig. 3(d)).

Furthermore, responsive NIR-II FL imaging of the vesicle was studied under excitation at 980 nm and emission at 1,550 nm. When excitation was performed in the absorption overlapping region (980 nm), the NIR-II FL signals of DCNP were quenched due to the energy filtration of excitation light by strong absorption of AuNNR (Fig. S5 in the ESM). The quenching process was reversed after the degradation of hybrid vesicles in an acidic environment (Fig. 3(e)). As expected, the NIR-II FL intensity of hybrid vesicles increased with increased aqueous solution acidity (Fig. 3(f)). These findings indicated that the hybrid vesicles had an excellent optical performance, and had great potential for activated NIR-II FL/NIR-II PA dual-modal imaging.

### 3.3 Intracellular drug release and radiotherapy

We next studied the DOX-loading and pH-triggered release performances of hybrid vesicles. Importantly, DOX was introduced into the internal space of the vesicles during the self-assembly process, and the loading content was dependent on the mass ratio between DOX and Ve. The DOX loading content of hybrid vesicles increased with the increasing feed ratio of AuNNR and DOX (Fig. 4(b)). Hybrid vesicles were well dispersed in DI water and exhibited high stability when the DOX loading content was 7%. Due to the disassembly behaviour of the vesicle in the acidic environment, DOX was slowly released and reached 60% at 48 h for the hybrid vesicle at pH 5.5 (Fig. 4(c)). Moreover, negligible drug release was observed from hybrid vesicles dispersed in a pH 7.4 phosphate-buffered saline (PBS) solution (Fig. 4(d)). The green and purple lines showed a very weak FL signal of DOX, due to the quenching effect of the DOX in the hybrid vesicle. However, with the pH-responsive disassembly and DOX release, the FL signals of

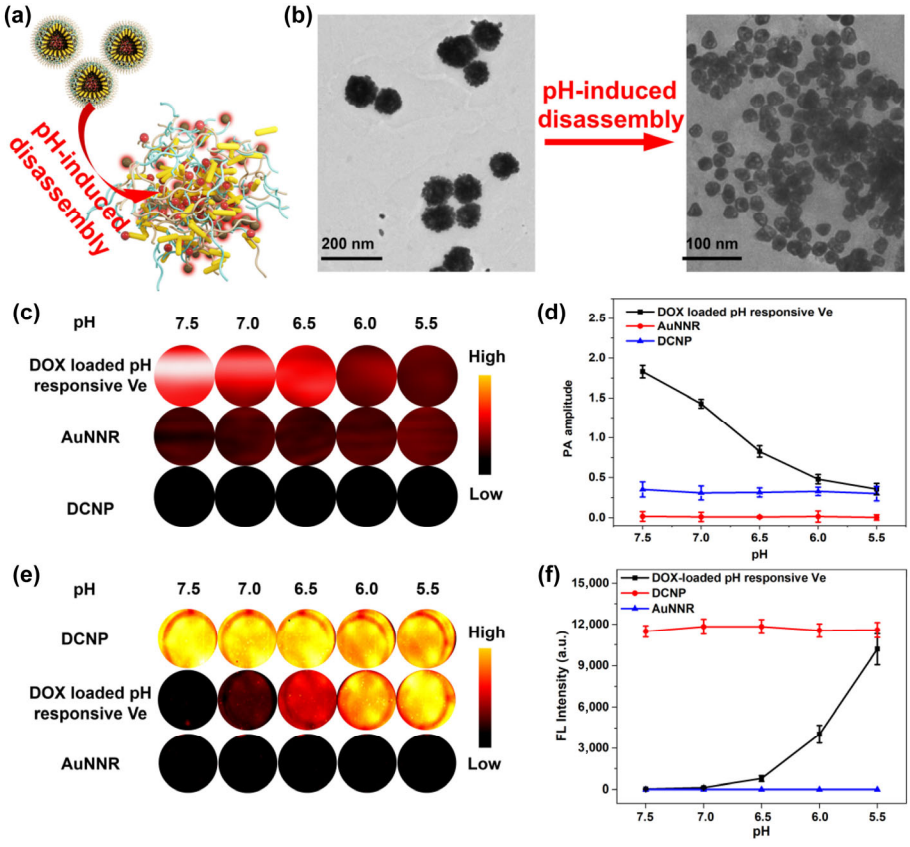


**Figure 3** (a) Schematic illustration of the pH-responsive process of the hybrid Ve. (b) TEM images of the vesicle before and after trigged by acidic environment. (c) NIR-II PA images and (d) PA amplitude of different samples in different pH solutions ($n$ = 3). (e) NIR-II FL images and (f) FL intensity of different samples at different pH under excitation at 980 nm laser ($n$ = 3).

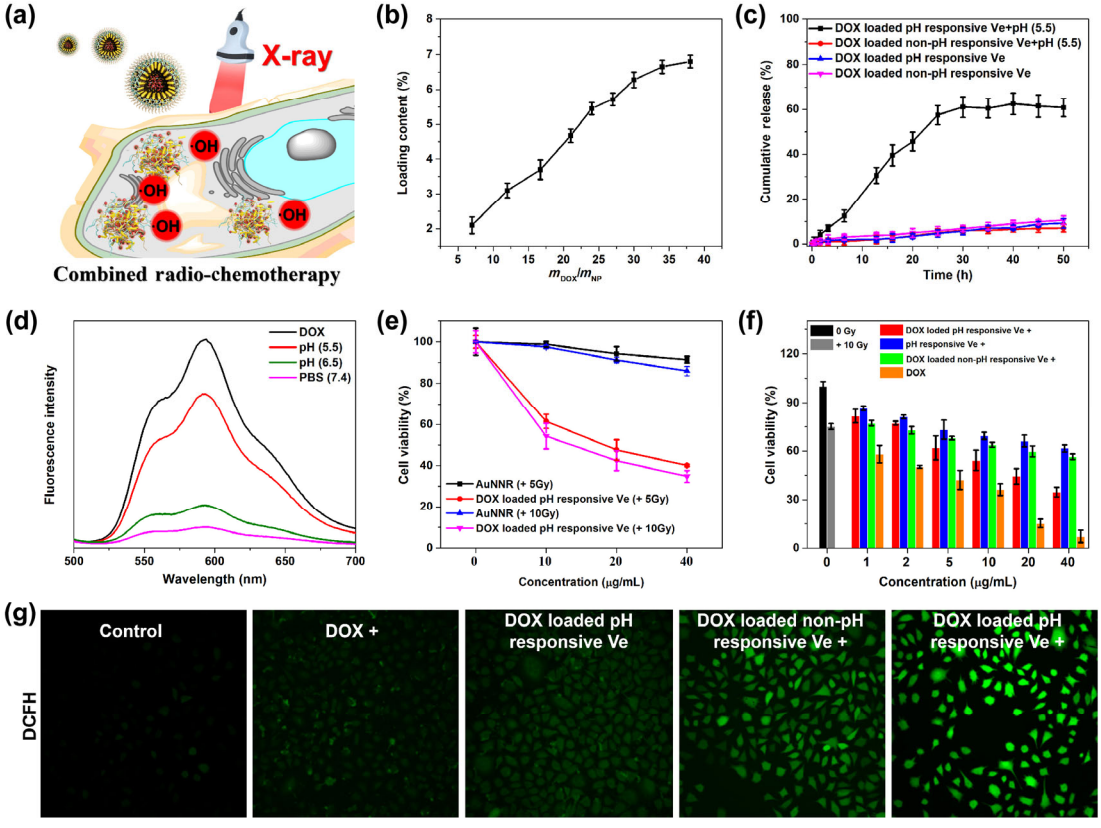


**Figure 4** (a) Schematic illustration of DOX-loaded hybrid vesicle for synergistic chemo-radiotherapy *in vitro*. (b) DOX-loaded content of the hybrid Ve. (c) Cumulative drug releasing profiles of the DOX loaded Ve in different pH solutions. (d) FL spectra of DOX in the responsive hybrid Ve in different pH solutions. (e) Concentration-dependent enhancement of irradiation cytotoxicity for both single AuNNR and DOX-loaded Ve. (f) Cell viability assay using MCF-7 cells at 24 h after incubation with different materials (X-ray: 10 Gy). The concentrations were normalized to DOX or gold. (g) Confocal microscopy images of cells with different treatments.

DOX in the hybrid vesicle were recovered at pH 5.5 (Fig. 4(d)). Interestingly, the negligible release of DOX and little change in hydrodynamic sizes after 24 h of incubation in plasma showed that DOX loaded Ve had excellent physiological stability (Fig. S7 in the ESM). Both AuNNR and DOX loaded Ve showed concentration-dependent elevation of cytotoxicity due to the irradiation sensitizers of AuNNR (Fig. 4(e)). Moreover, the effective pH-responsive DOX release performance and active targeting to the nucleus led to improved cytotoxicity of the hybrid vesicles, due to possible additive effects of both the released DOX and X-ray irradiation-generated ·OH.

Next, we evaluated the *in vitro* cytotoxicity of the DOX loaded vesicles. Except free DOX group, DOX loaded pH responsive Ve showed the higher cytotoxicity compared to none pH responsive DOX loaded Ve and free DOX irradiated with X-ray at 24 h post-irradiation(Fig. 4(f)). The hybrid vesicles also exhibited significant cytotoxicity at 48 h post-irradiation (5 and 10 Gy) (Fig. S8 in the ESM).

In addition, 2',7'-dichlorodihydrofluorescein diacetate ($H_2$DCFDA) was used to evaluate the sensitization ability of the hybrid vesicle with X-ray irradiation. In the presence of reactive oxygen species (ROS), the $H_2$DCFDA probe showed a green FL signal. Therefore, we further applied X-ray radiation to the hybrid vesicle, and observed that the green FL intensity of $H_2$DCFDA increased with increasing irradiation time (Fig. S10 in the ESM). The hybrid vesicles were subjected to X-ray irradiation on cells, and bright green FL of DCF was clearly observed, however no significant FL signal was observed in the control group (Fig. 4(g)). These results indicated that compared with X-ray alone, the ROS level was greatly elevated in the presence of the hybrid vesicles under X-ray irradiation. It is worth noting that cells treated with hybrid vesicles showed significant DOX-accumulation because of the release of free DOX triggered by acidic solution (Fig. S11(a) in the ESM). Conversely, the FL signal of DOX remained in the cytosol of cells treated with DOX-loaded Ve. DOX-loaded pH responsive Ve resulted in an average of 3.4-fold the FL intensity in the nucleus over DOX-loaded non-responsive Ve through semi-quantitative analysis, thereby illustrating the key role of the pH-response released DOX *in vitro* (Fig. S11(b) in the ESM). Taken together, the results showed that DOX-loaded Ve could be used as an effective pH-response drug carrier, and was an ideal material for initiating drug release and radiotherapy in the tumor microenvironment.

### 3.4 *In vivo* activated dual NIR-II FL and PA cancer imaging

The *in vivo* dual-mode NIR-II PA and FL imaging performances of the hybrid vesicle were further studied in MCF-7 tumor-bearing mice (Fig. 5(a)). The hybrid vesicle dissolved in a PBS solution (200 μL, 1 mg/mL) were injected into the tumor bearing mice via the tail vein. In brief, hybrid vesicles were intravenously injected into mice, and decay-related NIR-II PA and FL images were obtained after injection. At 1,250 nm, a significant PA signal was clearly observed in the tumor region at 4 h after injection of the Ve (Fig. 5(b)). The NIR-II PA signal increased until 16 h after injection and then slowly reduced. Because of the electron paramagnetic resonance (EPR) effect, the time course showed that hybrid vesicles continuously accumulated at the tumor site at 16 h post-injection. With pH-responses in the tumor microenvironment, the NIR-II FL signal was obvious at 8 h after injection (Ex 980 nm/*E*m 1,550 nm), which allowed for the evaluation of the delivery of the hybrid vesicles, and monitoring of the drug-release process in real-time. Moreover, the time-point of NIR-II FL imaging showed strong signal detection at the tumor region, while a low signal was observed at other sites over the course of time. Due to the high NIR-II FL signal of DCNP, the low tissue light absorption, and low background signal, the tumor region can clearly be visualized by NIR-II FL images with a high signal-to-noise ratio (Fig. S12 in the ESM).

The average NIR-II PA/FL intensity in the tumor area was consistent with the change in PA/FL signals of the tumor area (Fig. 5(d)). The changes in PA/FL signals could be explained through the competition between the metabolism and accumulation of hybrid vesicles in the tumor. Firstly, the intensity of the PA imaging reached its maximum value at about 16 h post-injection. Subsequently, the FL signal gradually increased until 48 h. Because the pH-responsive hybrid vesicles disassembled into single DCNP and AuNNR, the hybrid vesicle accumulation effect seemed to dominate. Decomposition of accumulated hybrid vesicles and metabolism may exceed accumulation of the hybrid vesicles, and after that, the disassembly of the hybrid vesicles involved dissociation into single AuNNR and DCNP. Importantly, the NIR-II PA signal was reduced due to the pH-responsive dissociation of hybrid vesicles in the tumor microenvironment, however, the signal at 970 nm was still strong, thereby indicating that the material was not completely metabolized out of the tumor and still had excellent imaging effects.

Compared with the PA spectrum of the hybrid Ve at 16 h post-injection, there was a significant blue-shift at 24 h post-injection, which further confirmed the disassembly of the hybrid Ve *in vivo* (Fig. 5(e)). However, an obvious PA signal and negligible FL signals were observed in the tumor area in the non-responsive Ve group (Fig. 5(c)). The NIR-II PA amplitude and FL intensity are presented in Fig. S13 in the ESM, which illustrated the enrichment of Ve in the tumor region, however, negligible NIR-II FL signal was observed in the tumor microenvironment, because of the non-responsive ability of the Ve. Moreover, the NIR-II FL intensity in the tumor was higher when compared to that of the liver region, indicating that pH-responsive hybrid vesicles showed specific tumor imaging ability (Fig. 5(f)). *Ex vivo* NIR-II FL images of the dissected tumors and major organs at 48 h post-injection also showed the specific tumor imaging performance of the DOX loaded pH responsive Ve (Figs. 5(g) and 5(h)).

Importantly, NIR-II PA and FL signals in the tumor area can be maintained for up to 40 h, which was consistent with *ex vivo* organ imaging results at 40 h post-injection (Fig. S13 in the ESM). In addition, it was noted that hybrid vesicles can be responsively dis-assembled into single AuNNR in the tumor microenvironment to deeply penetrate the tumor region. Under this dynamic process, the NIR-II PA signal could clearly be observed within the tumor region, and the location of tumor could accurately be imaged and guided radiotherapy reduced the damage to normal tissues. Importantly, after the disassembly of hybrid vesicles into single AuNNR and DCNP in the tumor microenvironment, the relatively smaller-sized nanoparticles could continue to deeply penetrate the tumor region and overcome the barriers of the tumor microenvironment, and can serve as a promising deep-tissue dual NIR-II PA and FL imaging agent for real-time *in vivo* investigation of the core of the tumor. Compared with non-pH responsive hybrid vesicles, pH responsive hybrid vesicles had a higher signal-to-noise ratio for pH-responsive NIR-II FL imaging, which can further aid subsequent NIR-II PA/FL imaging-guided cancer synergistic chemo-radiotherapy.

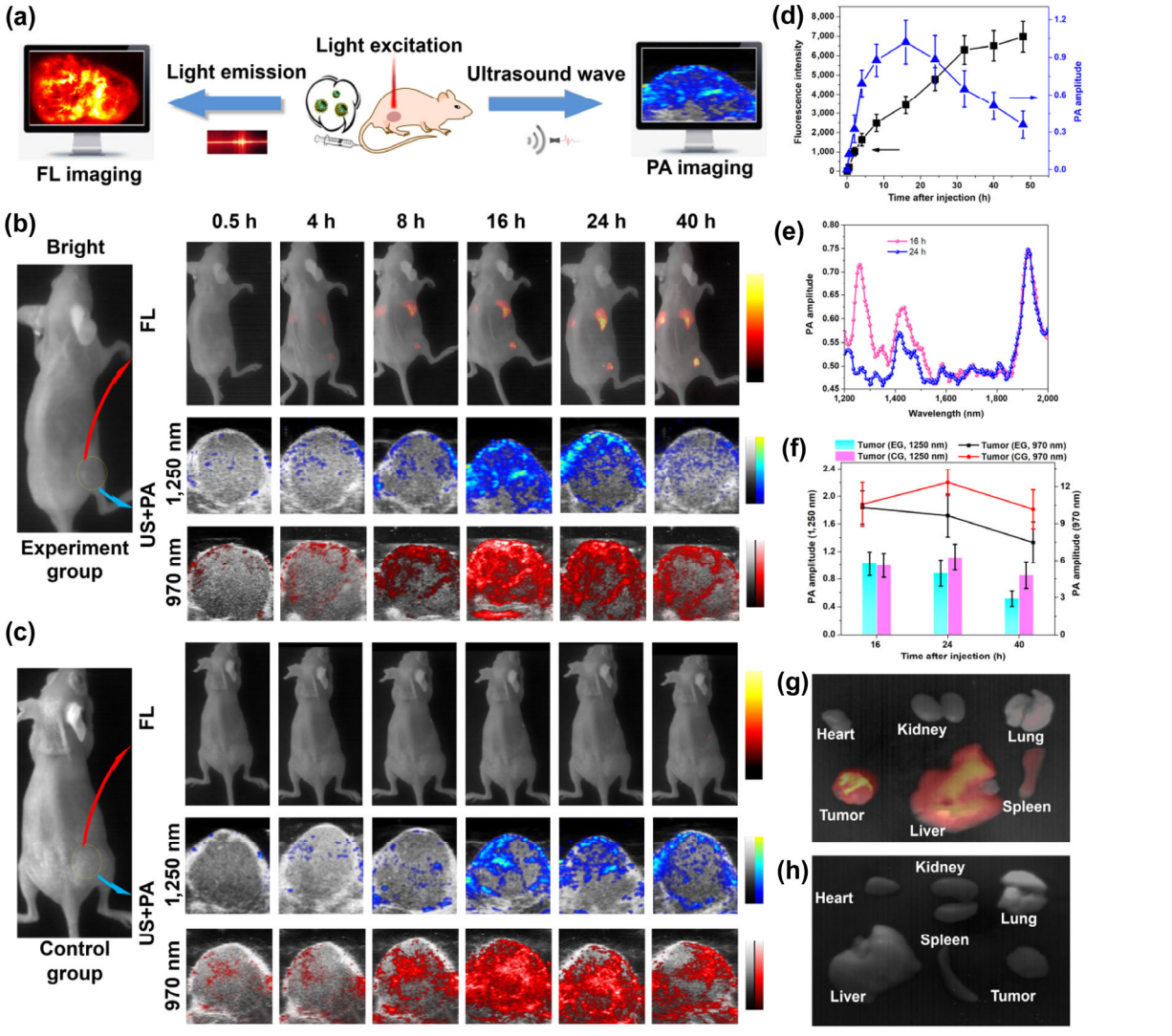


**Figure 5** (a) Schematic illustration of the hybrid vesicle used for cancer dual NIR-II PA and FL imaging. (b) NIR-II FL images and PA images of tumor bearing mice treated with the pH responsive Ve, (c) NIR-II FL images and PA images of MCF-7 cell bearing mice model after tail vein injection of none pH responsive hybrid Ve. (d) The FL intensity and PA amplitude of tumor treated with pH responsive Ve. (e) The PA spectra of tumors treated with none pH responsive hybrid Ve at post-injection 16 and 24 h, respectively. (f) The PA amplitude at 970 and 1,250 nm of tumor treated with the DOX loaded pH responsive hybrid Ve, DOX loaded non-pH responsive hybrid Ve, respectively. *Ex vivo* NIR-II fluorescence images of dissected tumors and major organs at 48 h post-injection of (g) DOX loaded pH responsive Ve and (h) DOX loaded non-pH responsive Ve, respectively.

### 3.5 Dual NIR-II PA/FL imaging-guided cancer synergistic chemotherapy and radiotherapy

To evaluate the chemo-radiotherapy effect of the DOX loaded hybrid Ve *in vivo*, we established a tumor model by subcutaneously injecting MCF-7 cells into the right rear flank of mice. Mice were randomly divided into 6 groups, and were administered different treatments before X-ray irradiation (5 and 10 Gy) at 24 h post-injection, including (1) PBS (control group), (2) DOX, (3) DOX + X-ray irradiation, (4) DOX loaded pH responsive Ve, (5) DOX loaded none pH responsive Ve + X-ray irradiation, and (6) DOX loaded pH responsive Ve + X-ray irradiation. The injected doses of the DOX, DOX loaded pH responsive Ve and DOX loaded none pH responsive Ve were 200 μL (40 μg/mL), 200 μL (1 mg/mL), and 200 μL (1 mg/mL), respectively. X-ray irradiation was applied at 24 h after i.v. injection of different formulations, and the tumor volume and survival rate were recorded until 18 and 32 days post-irradiation, respectively (Fig. 6(a)). The data showed that tumor growth was slightly delayed after X-ray irradiation in group (2) and (3). In group (4), the tumor growth was uncontrolled after irradiation, but slowed down in the first few days after irradiation. These data indicated that DOX release from the pH responsive Ve only had a limited treatment effect. The DOX loaded pH responsive Ve treated with X-ray irradiation in group 6 showed better cancer therapy effect compared with group 4 and group 5. It was because the DOX loaded pH responsive Ve received combined chemo-radiotherapy signifycantly and reduced tumor growth. Thus, these results showed that DOX loaded pH responsive Ve irradiated with X-ray had considerable radio-sensitization which overtly enhanced tumor growth inhibition, and realized simultaneous radiotherapy and chemotherapy to enhance the anti-cancer effect (Fig. 6(b)).

During treatment, no significant changes were observed in body weight, thereby indicating that the vesicles did not have a significant secondary action (Fig. 6(c)). The quantitative percentage of tumor volume inhibition of the group of mice that underwent DOX loaded pH responsive Ve + X-ray irradiation showed a conspicuous effective response over the other treatments at 18 days after treatment. In this group, three out of five mice were cured (only sacrificed for tissue examination) and survived for at least 32 days after treatment (Fig. 6(d)). More importantly, in the acidic tumor microenvironment, most of the hybrid vesicles injected were cleared

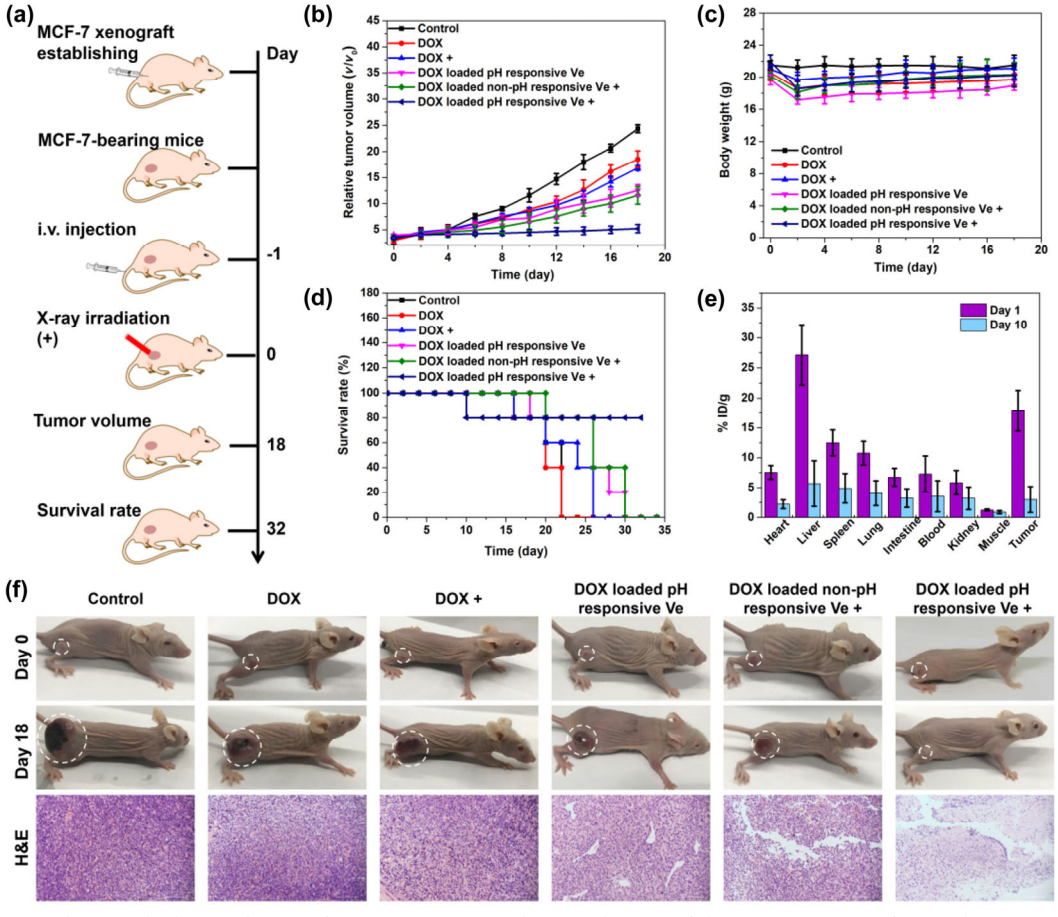


**Figure 6** Synergistic chemo-radiotherapy therapy of cancer *in vivo*. (a) Schematic diagram of the treating process of tumor bearing tumor, (b) tumor growth inhibition, (c) changes of mice body weight, and (d) animal survival curves after different treatments. (e) Biodistribution of Au element in major organs at day 1 and day 10 post-injection. (f) Photographs of dissected cancer tumors and images of hematoxylin and eosin (H&E) staining of tumor sections in different treatment groups.

from the body because most hybrid vesicles were dissociated into single AuNNR and DCNP at post-injection, and could easily be removed from the body (Fig. 6(e)). Hematoxylin and eosin (H&E) staining demonstrated that it has little toxicity to major organs after 18 days. H&E staining of tumor tissue showed significant necrosis (Fig. 6(f)). Therefore, the combination of radiotherapy and chemotherapy with DOX loaded pH responsive Ve induced massive apoptosis of tumor cells. In contrast, in the control group, histological staining of tumor tissue revealed many cells that underwent mitosis, which indicated the low treatment effect using either X-ray irradiation alone or DOX alone. Importantly, other organs of the treated mice did not show significant inflammation or tissue damage (Fig. S14 in the ESM), indicating that DOX loaded pH responsive Ve had great potential as bimodal NIR-II PA/FL theranostic agents for the diagnosis and treatment of tumors with excellent biocompatibility and safety profile.

## 4 Conclusion

In summary, we reported a novel plasmonic-fluorescent hybrid AuNNR-DCNP vesicle with pH responsive bimodal NIR-II PA/FL imaging performances for guiding cancer chemo-radiotherapy. Importantly, the encapsulated DOX in the hybrid vesicle resulted in an acid-responsive DOX release pattern, which was useful for bimodal NIR-II PA/FL imaging guided drug release. In addition, the tumor region showed an intense NIR-II PA/FL signal, because of the high accumulation and acid-responsiveness of hybrid vesicles in the tumor region. These properties allowed for thorough visualization of the shape and size of the tumor, and the radiation maximized radiotherapy and minimized the side effects of therapy to normal tissue. The pH responsive hybrid AuNNR-DCNP vesicle showed bimodal responsive NIR-II PA/FL imaging performances and had a synergistic cancer chemo-radiotherapy effect.

## Acknowledgements

This work was supported by the National Natural Science Foundation of China (Nos. 21635002 and 21874024), and the joint research projects of Health and Education Commission of Fujian Province (No. 2019-WJ-20).

**Electronic Supplementary Material**: Supplementary material (TEM, DLS, absorption spectrum, cell viability assay, NIR-II fluorescence images, and H&E staining) is available in the online version of this article at https://doi.org/10.1007/s12274-020-3000-9.

## References

[1] Chen, X. F.; Song, J. B.; Chen, X. Y.; Yang, H. H. X-ray-activated nanosystems for theranostic applications. *Chem. Soc. Rev.* **2019**, *48*, 3073–3101.

[2] Park, Y. I.; Lee, K. T.; Suh, Y. D.; Hyeon, T. Upconverting nanoparticles: A versatile platform for wide-field two-photon microscopy and multi-modal *in vivo* imaging. *Chem. Soc. Rev.* **2015**, *44*, 1302–1317.

[3] Cai, Y.; Wei, Z.; Song, C. H.; Tang, C. C.; Han, W.; Dong, X. C. Optical

nano-agents in the second near-infrared window for biomedical applications. *Chem. Soc. Rev.* **2019**, *48*, 22–37.
[4] Huang, X. L.; Song, J. B.; Yung, B. C.; Huang, X. H.; Xiong, Y. H.; Chen X. Y. Ratiometric optical nanoprobes enable accurate molecular detection and imaging. *Chem. Soc. Rev.* **2018**, *47*, 2873–2920.
[5] Zhou, Z. J.; Song, J. B.; Nie, L. M.; Chen, X. Y. Reactive oxygen species generating systems meeting challenges of photodynamic cancer therapy. *Chem. Soc. Rev.* **2016**, *45*, 6597–6626.
[6] Yang, L. J.; Zhou, Z. J.; Song, J. B.; Chen, X. Y. Anisotropic nanomaterials for shape-dependent physicochemical and biomedical applications. *Chem. Soc. Rev.* **2019**, *48*, 5140–5176.
[7] Fan, J.; He, Q. J.; Liu, Y.; Zhang, F. W.; Yang, X. Y.; Wang, Z.; Lu, N.; Fan, W. P.; Lin, L. S.; Niu, G. et al. Light-responsive biodegradable nanomedicine overcomes multidrug resistance via no-enhanced chemosensitization. *ACS Appl. Mater. Interfaces* **2016**, *8*, 13804–13811.
[8] Li, C. Y.; Wang, Q. B. Challenges and opportunities for intravital near-infrared fluorescence imaging technology in the second transparency window. *ACS Nano* **2018**, *12*, 9654–9659.
[9] Tsai, M. F.; Chang, S. H. G.; Cheng, F. Y.; Shanmugam, V.; Cheng, Y. S.; Su, C. H.; Yeh, C. S. Au nanorod design as light-absorber in the first and second biological near-infrared windows for *in vivo* photothermal therapy. *ACS Nano* **2013**, *7*, 5330–5342.
[10] Deng, H. Z.; Dong, A. J.; Song, J. B.; Chen, X. Y. Injectable thermosensitive hydrogel systems based on functional peg/pcl block polymer for local drug delivery. *J. Control. Release* **2019**, *297*, 60–70.
[11] Zhu, R.; Su, L. C.; Dai, J. Y.; Li, Z. W.; Bai, S. M.; Li, Q. Q.; Chen, X. Y.; Song, J. B.; Yang, H. H. Biologically responsive plasmonic assemblies for second near-infrared window photoacoustic imaging-guided concurrent chemo-immunotherapy. *ACS Nano* **2020**, *14*, 3991–4006.
[12] Jung, S.; Chen, X. Y. Quantum dot-dye conjugates for biosensing, imaging, and therapy. *Adv. Healthc Mater.* **2018**, *7*, 1800252.
[13] Barreto, J. A.; O'Malley, W.; Kubeil, M.; Graham, B.; Stephan, H.; Spiccia, L. Nanomaterials: Applications in cancer imaging and therapy. *Adv. Mater.* **2011**, *23*, H18–H40.
[14] Yao, C.; Wang, P. Y.; Li, X. M.; Hu, X. Y.; Hou, J. L.; Wang, L. Y.; Zhang, F. Near-infrared-triggered azobenzene-liposome/upconversion nanoparticle hybrid vesicles for remotely controlled drug delivery to overcome cancer multidrug resistance. *Adv. Mater.* **2016**, *28*, 9341–9348.
[15] Vankayala, R.; Hwang, K. C. Near-infrared-light-activatable nanomaterial-mediated phototheranostic nanomedicines: An emerging paradigm for cancer treatment. *Adv. Mater.* **2018**, *30*, 1706320.
[16] McHugh, K. J.; Jing, L. H.; Behrens, A. M.; Jayawardena, S.; Tang, W.; Gao, M. Y.; Langer, R.; Jaklenec, A. Biocompatible semiconductor quantum dots as cancer imaging agents. *Adv. Mater.* **2018**, *30*, 1706356.
[17] Li, Z.; Hu, Y. H.; Fu, Q. R.; Liu, Y.; Wang, J.; Song, J. B.; Yang, H. H. Nir/ros-responsive black phosphorus QD vesicles as immunoadjuvant carrier for specific cancer photodynamic immunotherapy. *Adv. Funct. Mater.* **2020**, *30*, 1905758.
[18] Liu, T. J.; Tong, L. L.; Lv, N. N.; Ge, X. G.; Fu, Q. R.; Gao, S.; Ma, Q. J.; Song, J. B. Two-stage size decrease and enhanced photoacoustic performance of stimuli-responsive polymer-gold nanorod assembly for increased tumor penetration. *Adv. Funct. Mater.* **2019**, *29*, 1806429.
[19] Lin, X. H.; Liu, S. Y.; Zhang, X.; Zhu, R.; Chen, S.; Chen, X. Y.; Song, J. B.; Yang, H. H. An ultrasound activated vesicle of Janus au-MnO nanoparticles for promoted tumor penetration and sono-chemodynamic therapy of orthotopic liver cancer. *Angew. Chem., Int. Ed.* **2020**, *59*, 1682–1688.
[20] Wang, S.; Lin, J.; Wang, T. F.; Chen, X. Y.; Huang, P. Recent advances in photoacoustic imaging for deep-tissue biomedical applications. *Theranostics* **2016**, *6*, 2394–2413.
[21] Zubkovs, V.; Antonucci, A.; Schuergers, N.; Lambert, B.; Latini, A.; Ceccarelli, R.; Santinelli, A.; Rogov, A.; Ciepielewski, D.; Boghossian, A. A. Spinning-disc confocal microscopy in the second near-infrared window (NIR-II). *Sci. Rep.* **2018**, *8*, 13770.
[22] Hong, G. S.; Antaris, A. L.; Dai, H. J. Near-infrared fluorophores for biomedical imaging. *Nat. Biomed. Eng.* **2017**, *1*, 0010.
[23] Song, J. B.; Lin, L. S.; Yang, Z.; Zhu, R.; Zhou, Z. J.; Li, Z. W.; Wang, F.; Chen, J. Y.; Yang, H. H.; Chen, X. Y. Self-assembled responsive bilayered vesicles with adjustable oxidative stress for enhanced cancer imaging and therapy. *J. Am. Chem. Soc.* **2019**, *141*, 8158–8170.
[24] Wei, J.; Sun, Z. K.; Luo, W.; Li, Y. H.; Elzatahry, A. A.; Al-Enizi, A. M.; Deng, Y. H.; Zhao, D. Y. New insight into the synthesis of large-pore ordered mesoporous materials. *J. Am. Chem. Soc.* **2017**, *139*, 1706–1713.
[25] Zhao, J. Y.; Zhong, D.; Zhou, S. B. NIR-I-to-NIR-II fluorescent nanomaterials for biomedical imaging and cancer therapy. *J. Mater. Chem. B* **2018**, *6*, 349–365.
[26] Fan, Q. L.; Cheng, K.; Yang, Z.; Zhang, R. P.; Yang, M.; Hu, X.; Ma, X. W.; Bu, L. H.; Lu, X. M.; Xiong, X. X. et al. Perylene-diimide-based nanoparticles as highly efficient photoacoustic agents for deep brain tumor imaging in living mice. *Adv. Mater.* **2015**, *27*, 843–847.
[27] Zhao, M. Y.; Li, B. H.; Wang, P. Y.; Lu, L. F.; Zhang, Z. C.; Liu, L.; Wang, S. F.; Li, D. D.; Wang, R.; Zhang, F. Supramolecularly engineered NIR-II and upconversion nanoparticles *in vivo* assembly and disassembly to improve bioimaging. *Adv. Mater.* **2018**, *30*, 1804982.
[28] Zhu, S. J.; Herraiz, S.; Yue, J. Y.; Zhang, M. X.; Wan, H.; Yang, Q. L.; Ma, Z. R.; Wang, Y.; He, J. H.; Antaris, A. L. et al. 3D NIR-II molecular imaging distinguishes targeted organs with high-performance NIR-II bioconjugates. *Adv. Mater.* **2018**, *30*, 1705799.
[29] Wang, Q.; Dai, Y. N.; Xu, J. Z.; Cai, J.; Niu, X. R.; Zhang, L.; Chen, R. F.; Shen, Q. M.; Huang, W.; Fan, Q. L. All-in-one phototheranostics: Single laser triggers NIR-II fluorescence/photoacoustic imaging guided photothermal/photodynamic/chemo combination therapy. *Adv. Funct. Mater.* **2019**, *29*, 1901480.
[30] Wen, Q. X.; Zhang, Y. J.; Li, C. Y.; Ling, S. S.; Yang, X. H.; Chen, G. C.; Yang, Y.; Wang, Q. B. NIR-II fluorescent self-assembled peptide nanochain for ultrasensitive detection of peritoneal metastasis. *Angew. Chem., Int. Ed.* **2019**, *58*, 11001–11006.
[31] Wang, S. F.; Liu, L.; Fan, Y.; El-Toni, A. M.; Alhoshan, M. S.; Li, D. D.; Zhang, F. *In vivo* high-resolution ratiometric fluorescence imaging of inflammation using NIR-II nanoprobes with 1550 nm emission. *Nano Lett.* **2019**, *19*, 2418–2427.
[32] Wang, P. Y.; Fan, Y.; Lu, L. F.; Liu, L.; Fan, L. L.; Zhao, M. Y.; Xie, Y.; Xu, C. J.; Zhang, F. NIR-II nanoprobes *in-vivo* assembly to improve image-guided surgery for metastatic ovarian cancer. *Nat. Commun.* **2018**, *9*, 2898.
[33] Zhang, W. M.; Chen, T.; Su, L. C.; Ge, X. G.; Chen, X. Y.; Song, J. B.; Yang, H. H. Quantum dot-based sensitization system for boosted photon absorption and enhanced second near-infrared luminescence of lanthanide-doped nanoparticle. *Anal. Chem.* **2020**, *92*, 6094–6102.
[34] Ceppi, L.; Bardhan, N. M.; Na, Y. J.; Siegel, A.; Rajan, N.; Fruscio, R.; Del Carmen, M. G.; Belcher, A. M.; Birrer, M. J. Real-time single-walled carbon nanotube-based fluorescence imaging improves survival after debulking surgery in an ovarian cancer model. *ACS Nano* **2019**, *13*, 5356–5365.
[35] Liu, J. J.; Wang, C.; Wang, X. J.; Wang, X.; Cheng, L.; Li, Y. G.; Liu, Z. Mesoporous silica coated single-walled carbon nanotubes as a multifunctional light-responsive platform for cancer combination therapy. *Adv. Funct. Mater.* **2015**, *25*, 384–392.
[36] Yu, G. C.; Yang, J.; Fu, X.; Wang, Z. T.; Shao, L.; Mao, Z. W.; Liu, Y. J.; Yang, Z.; Zhang, F. W.; Fan, W. P. et al. A supramolecular hybrid material constructed from graphene oxide and a pillar[6]arene-based host-guest complex as an ultrasound and photoacoustic signal nanoamplifier. *Mater. Horiz.* **2018**, *5*, 429–435.
[37] Naczynski, D. J.; Sun, C.; Turkcan, S.; Jenkins, C.; Koh, A. L.; Ikeda, D.; Pratx, G.; Xing, L. X-ray-induced shortwave infrared biomedical imaging using rare-earth nanoprobes. *Nano Lett.* **2015**, *15*, 96–102.
[38] Ai, X. Z.; Ho, C. J. H.; Aw, J.; Attia, A. B. E.; Mu, J.; Wang, Y.; Wang, X. Y.; Wang, Y.; Liu, X. G.; Chen, H. B. et al. *In vivo* covalent cross-linking of photon-converted rare-earth nanostructures for tumour localization and theranostics. *Nat. Commun.* **2016**, *7*, 10432.
[39] Wang, D. S.; Xie, T.; Qing, P.; Li, Y. D. Ag, $Ag_2S$, and $Ag_2Se$ nanocrystals: Synthesis, assembly, and construction of mesoporous structures. *J. Am. Chem. Soc.* **2008**, *130*, 4016–4022.
[40] Robinson, J. T.; Hong, G. S.; Liang, Y. Y.; Zhang, B.; Yaghi, O. K.; Dai, H. J. *In vivo* fluorescence imaging in the second near-infrared

window with long circulating carbon nanotubes capable of ultrahigh tumor uptake. *J. Am. Chem. Soc.* **2012**, *134*, 10664–10669.

[41] Tang, W.; Yang, Z.; Wang, S.; Wang, Z. T.; Song, J. B.; Yu, G. C.; Fan, W. P.; Dai, Y. L.; Wang, J. J.; Shan, L. L. et al. Organic semiconducting photoacoustic nanodroplets for laser-activatable ultrasound imaging and combinational cancer therapy. *ACS Nano* **2018**, *12*, 2610–2622.

[42] Hao, X. X.; Li, C. Y.; Zhang, Y. J.; Wang, H. Z.; Chen, G. C.; Wang, M.; Wang, Q. B. Programmable chemotherapy and immunotherapy against breast cancer guided by multiplexed fluorescence imaging in the second near-infrared window. *Adv. Mater.* **2018**, *30*, 1804437.

[43] Yang, X. Y.; Wang, Z.; Zhang, F. W.; Zhu, G. Z.; Song, J. B.; Teng, G. J.; Niu, G.; Chen, X. Y. Mapping sentinel lymph node metastasis by dual-probe optical imaging. *Theranostics* **2017**, *7*, 153–163.

[44] Ren, F.; Ding, L. H.; Liu, H. H.; Huang, Q.; Zhang, H.; Zhang, L. J.; Zeng, J. F.; Sun, Q.; Li, Z.; Gao, M. Y. Ultra-small nanocluster mediated synthesis of $Nd^{3+}$-doped core-shell nanocrystals with emission in the second near-infrared window for multimodal imaging of tumor vasculature. *Biomaterials* **2018**, *175*, 30–43.

[45] Fu, Q. R.; Li, Z.; Ye, J. M.; Li, Z.; Fu, F. F.; Lin, S. L.; Chang, C. A.; Yang, H. H.; Song, J. B. Magnetic targeted near-infrared II PA/MR imaging guided photothermal therapy to trigger cancer immunotherapy. *Theranostics* **2020**, *10*, 4997–5010.

[46] Cui, D.; Huang, J. G.; Zhen, X.; Li, J. C.; Jiang, Y. Y. A semiconducting polymer nano-prodrug for hypoxia-activated photodynamic cancer therapy. *Angew. Chem., Int. Ed.* **2019**, *58*, 5920–5924.

[47] Deng, H. Z.; Lin, L. S.; Wang, S.; Yu, G. C.; Zhou, Z. J.; Liu, Y. J.; Niu, G.; Song, J. B.; Chen, X. Y. X-ray-controlled bilayer permeability of bionic nanocapsules stabilized by nucleobase pairing interactions for pulsatile drug delivery. *Adv. Mater.* **2019**, *31*, 1903443.

[48] Kenry; Duan, Y. K.; Liu, B. Recent advances of optical imaging in the second near-infrared window. *Adv. Mater.* **2018**, *30*, 1802394.

[49] Wu, Y.; Guo, T.; Qiu, Y.; Lin, Y.; Yao, Y. Y.; Lian, W. B.; Lin, L. S.; Song, J. B.; Yang, H. H. An inorganic prodrug, tellurium nanowires with enhanced ros generation and gsh depletion for selective cancer therapy. *Chem. Sci.* **2019**, *10*, 7068–7075.

[50] Maldonado, C. R.; Salassa, L.; Gomez-Blanco, N.; Mareque-Rivas, J. C. Nano-functionalization of metal complexes for molecular imaging and anticancer therapy. *Coordin. Chem. Rev.* **2013**, *257*, 2668–2688.

[51] Wang, P. Y.; Wang, X. D.; Luo, Q.; Li, Y.; Lin, X. X.; Fan, L. L.; Zhang, Y.; Liu, J. F.; Liu, X. L. Fabrication of red blood cell-based multimodal theranostic probes for second near-infrared window fluorescence imaging-guided tumor surgery and photodynamic therapy. *Theranostics* **2019**, *9*, 369–380.

[52] Lu, K. D.; He, C. B.; Guo, N. N.; Chan, C.; Ni, K. Y.; Lan, G. X.; Tang, H. D.; Pelizzari, C.; Fu, Y. X.; Spiotto, M. T. et al. Low-dose X-ray radiotherapy–radiodynamic therapy via nanoscale metal–organic frameworks enhances checkpoint blockade immunotherapy. *Nat. Biomed. Eng.* **2018**, *2*, 600–610.

[53] Liu, J.; Cai, X. L.; Pan, H. C.; Bandla, A.; Chuan, C. K.; Wang, S. W.; Thakor, N.; Liao, L. D.; Liu, B. Molecular engineering of photoacoustic performance by chalcogenide variation in conjugated polymer nanoparticles for brain vascular imaging. *Small* **2018**, *14*, 1703732.

[54] Du, Z.; Zhang, X.; Guo, Z.; Xie, J. N.; Dong, X. H.; Zhu, S.; Du, J. F.; Gu, Z. J.; Zhao, Y. L. X-ray-controlled generation of peroxynitrite based on nanosized $LiLuF_4$: $Ce^{3+}$ scintillators and their applications for radiosensitization. *Adv. Mater.* **2018**, *30*, 1804046.

[55] Jiang, Y.; Upputuri, P. K.; Xie, C.; Zeng, Z. L.; Sharma, A.; Zhen, X.; Li, J. C.; Huang, J. G.; Pramanik, M.; Pu, K. Y. Metabolizable semiconducting polymer nanoparticles for second near-infrared photoacoustic imaging. *Adv. Mater.* **2019**, *31*, 1808166.

[56] Zhou, L. B.; Jing, Y.; Liu, Y. B.; Liu, Z. H.; Gao, D. Y.; Chen, H. B.; Song, W. Y.; Wang, T.; Fang, X. F.; Qin, W. P. et al. Mesoporous carbon nanospheres as a multifunctional carrier for cancer theranostics. *Theranostics* **2018**, *8*, 663–675.

[57] Yang, Z.; Song, J. B.; Dai, Y. L.; Chen, J. Y.; Wang, F.; Lin, L. S.; Liu, Y. J.; Zhang, F. W.; Yu, G. C.; Zhou, Z. J. et al. Self-assembly of semiconducting-plasmonic gold nanoparticles with enhanced optical property for photoacoustic imaging and photothermal therapy. *Theranostics* **2017**, *7*, 2177–2185.

[58] Sun, W. J.; Shi, T. H.; Luo, L.; Chen, X. M.; Lv, P.; Lv, Y.; Zhuang, Y. X.; Zhu, J. J.; Liu, G.; Chen, X. Y. et al. Monodisperse and uniform mesoporous silicate nanosensitizers achieve low-dose X-ray-induced deep-penetrating photodynamic therapy. *Adv. Mater.* **2019**, *31*, 1808024.

[59] Ge, X. G.; Fu, Q. R.; Su, L. C.; Li, Z.; Zhang, W. M.; Chen, T.; Yang, H. H.; Song, J. B. Light-activated gold nanorod vesicles with NIR-II fluorescence and photoacoustic imaging performances for cancer theranostics. *Theranostics* **2020**, *10*, 4809–4821.